

# Extracting near-field seismograms from ocean-bottom pressure gauge inside the focal area: application to the 2011 Mw 9.0 Tohoku-Oki earthquake

Tatsuya Kubota<sup>1</sup>, Tatsuhiko Saito<sup>1</sup>, Hiroaki Tsushima<sup>2</sup>, Ryota Hino<sup>3</sup>, Yusaku Ohta<sup>3</sup>, Syuichi Suzuki<sup>3</sup>, and Daisuke Inazu<sup>4</sup>

<sup>1</sup>National Research Institute for Earth Science and Disaster Resilience

<sup>2</sup>Meteorological Research Institute

<sup>3</sup>Tohoku University

<sup>4</sup>Tokyo University of Marine Science and Technology

November 23, 2022

## Abstract

Recent studies have shown that ocean-bottom pressure gauges (OBPs) can record seismic waves in addition to tsunamis and seafloor permanent displacements, even if they are installed inside the focal area where the signals are extremely large. We developed a method to extract dynamic ground motion waveforms from near-field OBP data consisting of a complex mixture of various signals, based on an inversion analysis along with a theory of tsunami generation. We applied this method to the OBP data of the 2011 Tohoku-Oki earthquake. We successfully extracted the low-frequency vertical seismograms inside the focal area ( $f < \sim 0.05$  Hz), although those of the Mw  $\sim 9.0$  megathrust earthquake had never previously been reported. The seismograms suggested two dominant energy releases around the hypocenter. The seismic wave signals recorded by the near-field OBP will be important not only to reveal earthquake ruptures and tsunami generation processes but also to conduct real-time tsunami forecasts.



*Geophysical Research Letters*

Supporting Information for

**Extracting near-field seismogram from ocean-bottom pressure gauge inside the focal area: application to the 2011 Mw 9.0 Tohoku-Oki earthquake**

T. Kubota<sup>1</sup>, T. Saito<sup>1</sup>, H. Tsushima<sup>2</sup>, R. Hino<sup>3</sup>, Y. Ohta<sup>3</sup>, S. Suzuki<sup>3</sup>, D. Inazu<sup>4</sup>

<sup>1</sup> National Research Institute for Earth Science and Disaster Resilience, Tsukuba, Japan <sup>2</sup> Meteorological Research Institute, Japan Meteorological Agency, Tsukuba, Japan <sup>3</sup> Graduate School of Science, Tohoku University, Sendai, Japan <sup>4</sup> Department of Marine Resources and Energy, Tokyo University of Marine Science and Technology, Tokyo, Japan

## Contents of this file

Figures S1 to S3 Table S1

### Introduction

Calculation of the hydrostatic and dynamic pressure changes from the inversion result is shown in Figure S1. Comparison of the amplitude spectra at GJT3 is shown in Figure S2. Figure S3 compares the seismograms obtained by this study and those expected from the bandpass filter. The station list is shown in Table S1.

### Hosted file

image2.emf available at <https://authorea.com/users/543755/articles/601386-extracting-near-field-seismograms-from-ocean-bottom-pressure-gauge-inside-the-focal-area-application-to-the-2011-mw-9-0-tohoku-oki-earthquake>

**Figure S1.** Comparison between the observed pressure waveforms (black) with the simulated waveforms, for (a,b) dynamic (green), (c, d) hydrostatic (blue), and (e,f) both pressure changes.

### Hosted file

image3.emf available at <https://authorea.com/users/543755/articles/601386-extracting-near-field-seismograms-from-ocean-bottom-pressure-gauge-inside-the-focal-area-application-to-the-2011-mw-9-0-tohoku-oki-earthquake>

**Figure S2.** Comparison of spectral amplitudes at GJT3 between the observed one (black) and calculated ones; red: both hydrostatic and dynamic, blue: only hydrostatic, green: only dynamic pressure changes. The time window of 2048 s from the origin time is used for the spectral calculation.

### Hosted file

image4.emf available at <https://authorea.com/users/543755/articles/601386-extracting-near-field-seismograms-from-ocean-bottom-pressure-gauge-inside-the-focal-area-application-to-the-2011-mw-9-0-tohoku-oki-earthquake>

**Figure S3.** Comparison between the extracted seismograms (red), and the lowpass-filtered (0.05 Hz, gray) and the bandpass-filtered (0.01–0.05 Hz, black dashed) waveforms, for (a) vertical acceleration and (b) vertical displacement.

**Table S1.** List of the stations used in this study.<sup>a</sup>

Station	Latitude [°N]	Longitude [°E]	Depth [m]	Inversion time window [s]	Agency
GJT3	38.2945	143.4814	3293	0 – 3600	Tohoku University
P02	38.5002	142.5016	1104	0 – 3600	Tohoku University
P03	38.1834	142.3998	1052	0 – 3600	Tohoku University
P06	38.6340	142.5838	1254	0 – 3600	Tohoku University
P07	38.0003	142.4488	1059	0 – 3600	Tohoku University
P08	38.2855	142.8330	1418	0 – 3600	Tohoku University
P09	38.2659	143.0006	1556	0 – 3600	Tohoku University
TM1	39.2312	142.7684	1618	0 – 1800	ERI
TM2	39.2489	142.4412	1013	0 – 1800	ERI

<sup>a</sup>All data were resampled to 1 Hz after the filtering process.

1       **Extracting near-field seismograms from ocean-bottom pressure gauge inside the**  
2       **focal area: application to the 2011 Mw 9.0 Tohoku-Oki earthquake**

3  
4       **T. Kubota<sup>1</sup>, T. Saito<sup>1</sup>, H. Tsushima<sup>2</sup>, R. Hino<sup>3</sup>, Y. Ohta<sup>3</sup>, S. Suzuki<sup>3</sup>, D. Inazu<sup>4</sup>**  
5

6       <sup>1</sup> National Research Institute for Earth Science and Disaster Resilience, Tsukuba, Japan

7       <sup>2</sup> Meteorological Research Institute, Japan Meteorological Agency, Tsukuba, Japan

8       <sup>3</sup> Graduate School of Science, Tohoku University, Sendai, Japan

9       <sup>4</sup> Department of Marine Resources and Energy, Tokyo University of Marine Science and  
10       Technology, Tokyo, Japan

11  
12       Corresponding author: Tatsuya Kubota (kubotatsu@bosai.go.jp)

13  
14       **Key Points:**

- 15       • We develop a method to extract low-frequency ground motion including permanent  
16       deformation from ocean-bottom pressure gauge (OBP) data
- 17       • We obtain the seismograms inside the focal area of the 2011 Tohoku-Oki EQ, which  
18       suggest two dominant energy releases around the hypocenter
- 19       • High-frequency near-field OBP signals should be utilized more widely for geophysical  
20       research as well as real-time tsunami forecasting  
21

**Abstract**

Recent studies have shown that ocean-bottom pressure gauges (OBPs) can record seismic waves in addition to tsunamis and seafloor permanent displacements, even if they are installed inside the focal area where the signals are extremely large. We developed a method to extract dynamic ground motion waveforms from near-field OBP data consisting of a complex mixture of various signals, based on an inversion analysis along with a theory of tsunami generation. We applied this method to the OBP data of the 2011 Tohoku-Oki earthquake. We successfully extracted the low-frequency vertical seismograms inside the focal area ( $f < \sim 0.05$  Hz), although those of the  $M_w \sim 9.0$  megathrust earthquake had never previously been reported. The seismograms suggested two dominant energy releases around the hypocenter. The seismic wave signals recorded by the near-field OBP will be important not only to reveal earthquake ruptures and tsunami generation processes but also to conduct real-time tsunami forecasts.

**Plain Language Summary**

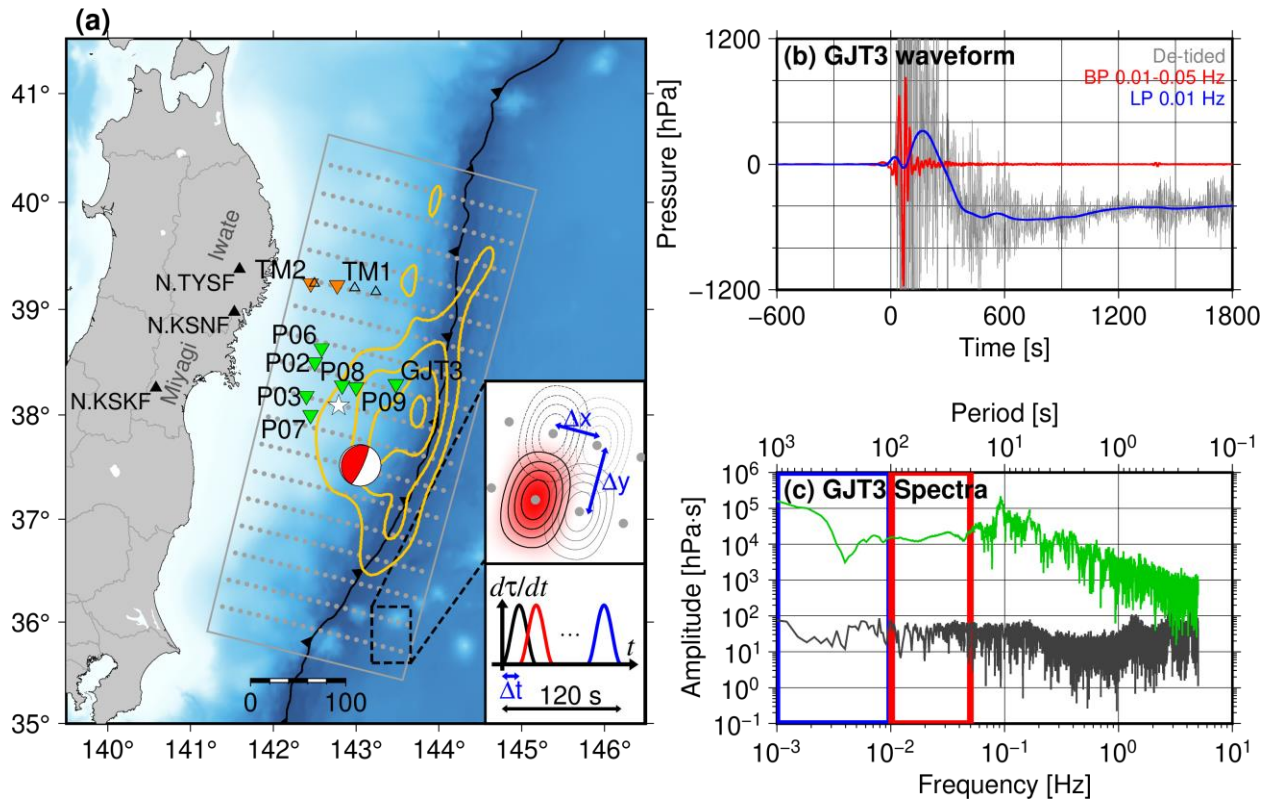
During tsunami generation, different types of waves such as ground motions, ocean acoustic waves, and tsunamis coexist inside the focal area, forming complicated wavefields and pressure changes at the sea bottom. This study developed a method to appropriately decompose the complicated ocean-bottom pressure gauge (OBP) waveforms into ground motion and tsunami signals. Our method was applied to the near-field OBP data of the 2011 Tohoku-Oki earthquake to extract the near-field seismic motion waveform which had never been reported previously. The waveform suggested a complex earthquake rupture process along the plate boundary, in which the rupture happened twice near the hypocenter. The seismic wave signals recorded by the near-field OBP will be important not only to reveal the processes of the earthquake rupture and tsunami generation but also to issue tsunami alarms.

## 47 **1 Introduction**

48 Seismic observations are very important to estimate earthquake source parameters and  
49 physical properties around the fault and to understand how an earthquake plays a role in  
50 geodynamic frameworks. Far-field seismograms have been used for earthquake kinematic  
51 rupture modeling (e.g., Lay et al., 2011). Near-field seismograms are also essential to resolve the  
52 rupture kinematics, because far-field seismograms are affected by path effects such as  
53 attenuation and scattering and resolve very little about the short-wavelength information on the  
54 source (e.g., Aki & Richards, 2002). Near-fault seismograms are also important for earthquake  
55 rupture dynamics. Stress drop, defined as shear stress reduction on the fault due to an earthquake,  
56 and slip weakening distance  $D_c$ , the slip amount needed to reach residual friction, are often  
57 inferred from near-field seismograms (e.g., Ide & Takeo, 1997; Mikumo et al., 2003; Fukuyama  
58 & Mikumo, 2007; Fukuyama & Suzuki, 2016; Kaneko et al., 2017).

59 In the 2011 Tohoku-Oki earthquake (Mw 9.0, Global Centroid Moment Tensor  
60 [GCMT]; hereafter, the mainshock), various near-field observations were recorded, which were  
61 not obtained for past megathrust earthquakes (e.g., Hino, 2015; Lay, 2018; Wang et al., 2018;  
62 Kodaira et al., 2020). Seafloor geodetic observations (e.g., Fujiwara et al., 2011; 2017; Ito et al.,  
63 2011; Kido et al., 2011; Sato et al., 2011) have particularly played an important role in revealing  
64 the mainshock rupture process and tsunami generation (e.g., Iinuma et al., 2012). However, near-  
65 field seismograms associated with the mainshock with a reasonable quality have not been  
66 reported. The high-sensitivity ocean-bottom seismometers (OBSs) installed off Miyagi (Suzuki  
67 et al., 2012) went off-scale and whole seismograms were not recorded. The strong motion  
68 accelerometers installed outside of the main rupture area (open triangles in Figure 1a) were  
69 dynamically rotated by the strong shaking (Nakamura & Hayashimoto, 2019). Although some  
70 near-source seismograms during past megathrust earthquakes have been recorded by onshore  
71 seismometers and GNSS, such as in the 2010 and 2014 Chile earthquakes (Vigny et al., 2011;  
72 Madariaga et al., 2019), the stations were located outside of the main rupture regions, where the  
73 permanent displacement was small.

74



75

76 **Figure 1.** (a) Location map of this study. Inverted triangles denote OBPs (green: Tohoku  
 77 University, orange: ERI). Open triangles denote OBS stations by ERI. Black triangles are the F-  
 78 net onshore seismometers. The white star is the mainshock epicenter (Suzuki et al., 2012) and the  
 79 red CMT solution is taken from GCMT. Yellow contours denote the distributions of the initial  
 80 tsunami height (Saito et al., 2011, 2 m interval). Gray dots and rectangular areas indicate the  
 81 locations of the unit sources and the analytical area of the inversion analysis. The configuration  
 82 of the unit sources in the space and time domains is schematically shown in the inset. (b)  
 83 Pressure waveforms at GJT3. Gray, red, and blue traces are the de-tided, bandpass filtered (0.01–  
 84 0.05 Hz), and lowpass filtered (0.01 Hz) waveforms, respectively. (c) Spectral amplitude before  
 85 and after the mainshock (black and green, respectively), calculated based on Aki and Richards’  
 86 (2002) definition. Passbands of the filters in Figure 1b are marked by colored rectangles.

87

88 During the mainshock, some ocean-bottom pressure gauges (OBPs) were installed  
 89 around the main rupture area (inverted triangles in Figure 1). The deep-ocean OBPs often  
 90 observe tsunamis, which have dominant frequencies lower than  $\sim 0.01$  Hz. Such tsunami data  
 91 have been widely utilized, because tsunamis constrain the spatial extent of the seafloor vertical  
 92 deformation (tsunami source) better than seismic waves (Kubota et al., 2018). This is attributed  
 93 to tsunamis’ much slower propagation velocity and there being a less significant tradeoff  
 94 between the source dimension and rupture propagation velocity across the fault. Previous studies  
 95 used the mainshock OBP data to investigate the mainshock tsunami generation process (e.g.,  
 96 Saito et al., 2011 (yellow contour lines in Figure 1a); Maeda et al., 2011; Tsushima et al., 2011;

97 Gusman et al., 2012; Satake et al., 2013; Baba et al., 2015; Hossen et al., 2015; Dettmer et al.,  
 98 2016; Yamazaki et al., 2018). However, they did not utilize the OBPs installed inside the main  
 99 tsunami source region where the seafloor uplift was extremely large (e.g., GJT3, Figure 1). This  
 100 is mainly because there have been few near-field observation examples (e.g., Mikada et al.,  
 101 2006) and the method to utilize the permanent deformation for tsunami modeling was not  
 102 established. In this decade, the well-established method to utilize the permanent deformation for  
 103 tsunami modeling was proposed (Tsushima et al., 2012) and many finite fault models using the  
 104 OBPs inside the tsunami source have been obtained (e.g., Kubota, Hino et al., 2017; Nemoto et  
 105 al., 2019).

106 Our understanding of the ocean-bottom pressure change inside the focal area has also  
 107 progressed by various theoretical and observational studies. In addition to tsunamis and  
 108 permanent seafloor deformation, OBPs observe seismic wave signals with dominant frequency  
 109 of  $> \sim 10^{-2}$  Hz (e.g., Filloux, 1982; Webb, 1998; Nosov and Kolesov, 2007; Matsumoto et al.,  
 110 2012; 2017; Saito & Tsushima, 2016; An et al., 2017; Kubota, Saito et al., 2017; Saito, 2019; Ito  
 111 et al., 2020; Mizutani et al., 2020; Saito & Kubota, 2020). These seismic waves in the OBP have  
 112 reasonable signal-to-noise ratio for the purposes of various geophysical analyses (Kubota et al.,  
 113 2020), such as earthquake source parameter estimations (An et al., 2017; Kubota, Saito et al.,  
 114 2017). However, it has also been reported that a simple bandpass filter cannot extract the seismic  
 115 waves from the complex pressure change field inside the focal area (Saito & Tsushima, 2016). A  
 116 method to appropriately decompose the OBP signal to the seismic and tsunami signals is not  
 117 established yet.

118 The purpose of this study is to propose a method to appropriately extract the seafloor  
 119 dynamic motion time series from the near-field OBP data inside the focal area. To achieve this,  
 120 we attempt to decompose the OBP signals into seismic and tsunami wave signals based on a  
 121 tsunami generation theory. Section 2 describes a theory of tsunami generation inside the focal  
 122 area, the mainshock OBP data used in this study, and the procedure of our method. In section 3,  
 123 we show the results of the application of the method to the mainshock OBP data. Discussion and  
 124 summary of this study are given in sections 4 and 5, respectively.

125

## 126 **2 Data and Methods**

### 127 2.1 Ocean-bottom pressure inside the focal area

128 We represent the ocean-bottom pressure change inside the focal area as the sum of the  
 129 contribution originating due to gravity ( $p_{\text{gravity}}(t)$ ) and that without gravity  $p_{\text{non-gravity}}(t)$   
 130 (Saito, 2019):

131

$$132 \quad p(t) = p_{\text{gravity}}(t) + p_{\text{non-gravity}}(t). \quad (1)$$

133

134 Supposing that the wave period is long, we may consider the seawater as an incompressible fluid.

135 Also supposing that the sea-surface height change is small enough compared to the water depth  
 136 and that the wavelength is much longer than the sea depth,  $p_{\text{gravity}}(t)$  is approximately given by

$$137$$

$$138 \quad p_{\text{gravity}}(t) \approx p_{\text{hydrostatic}}(t) = \rho_0 g_0 [\eta(t) - u_z(t)], \quad (2)$$

139  
 140 where  $\rho_0 = 1030 \text{ kg/m}^3$  and  $g_0 = 9.8 \text{ m/s}^2$  are the seawater density and gravity acceleration,  
 141 and  $\eta(t)$  and  $f(t)$  are the time series of the sea-surface height change (tsunami) and the seafloor  
 142 vertically upward displacement, respectively. Hereinafter we refer to  $p_{\text{hydrostatic}}(t)$  as the  
 143 hydrostatic pressure change. The pressure change without gravity can be approximated as the  
 144 dynamic pressure change, related to the action-reaction forces of the vertically accelerating  
 145 seafloor, as

$$146$$

$$147 \quad p_{\text{non-gravity}}(t) \approx p_{\text{dynamic}}(t) = \rho_0 h_0 \frac{d^2 u_z(t)}{dt^2}, \quad (3)$$

148  
 149 where  $h_0$  is seawater depth. This relationship is basically valid at frequencies lower than the  
 150 acoustic resonant frequency  $f_0 = c_0/4h_0$  ( $c_0$ : ocean-acoustic wave velocity). In this study, we  
 151 attempt to extract the vertical acceleration  $d^2 u_z/dt^2$  from the pressure change  $p(t)$ .

## 152

### 153 2.2 OBP data

154 We use seven OBPs installed off Miyagi by Tohoku University (green inverted triangles  
 155 in Figure 1a), which utilize Paroscientific Digiquartz precise quartz pressure sensors, 8B7000  
 156 series (Hino et al., 2014). We also use two cabled OBPs installed off Iwate by the Earthquake  
 157 Research Institute (ERI), the University of Tokyo (orange inverted triangles), which use the  
 158 quartz pressure sensor manufactured by Hewlett-Packard Inc. (Kanazawa & Hasegawa, 1997;  
 159 Maeda et al., 2011). Although the frequency response of a quartz pressure sensor generally  
 160 depends on the counting method of the quartz oscillation, the response of the quartz pressure  
 161 sensor is typically flat at lower frequency band of  $< \sim 1$  Hz regardless of its counting method  
 162 (Webb & Nooner, 2016). Station locations are listed in Table S1.

163 We subtract the tidal components using the model of Matsumoto et al. (2000) to remove  
 164 ocean tides. We then apply a 4th-order Butterworth lowpass filter with a cutoff of 0.05 Hz in  
 165 both forward and backward directions to reduce higher-frequency ocean-acoustic wave  
 166 components. The cutoff of 0.05 Hz is determined considering the acoustic resonant frequency  $f_0$   
 167 for the OBP at GJT3 ( $\sim 0.11$  Hz). All records are resampled to 1 Hz after the filtering.

168 The de-tided waveform at GJT3 is shown in Figure 1b (gray trace). In Figure 1c, spectral  
 169 amplitudes of the de-tided records before and after the mainshock are shown, which are  
 170 calculated based on Aki and Richards' (2002) definition (time windows of 3276.8 s are used).  
 171 High-frequency ocean-acoustic wave signals can be recognized even 1800 s after the origin time,  
 172 and are dominant in frequencies higher than the acoustic resonant frequency  $f_0 \sim 0.11$  Hz.

173 Dynamic pressure changes (Eq. (3)) are evident during the first few minutes, particularly for the  
 174 frequency range 0.01–0.05 Hz (red traces in Figure 1b). Subsequently, low-frequency hydrostatic  
 175 pressure changes (Eq. (2)) are also confirmed ( $< 0.01$  Hz, blue).

176

### 177 2.3 Extracting ground motions from OBP data

178 This study attempts to extract the vertical acceleration  $d^2u_z/dt^2$  in Eq. (3) from the  
 179 OBP data. In other words, our goal is to appropriately decompose the observed pressure change  
 180 into its hydrostatic and dynamic components. To achieve this, we develop a method based on the  
 181 inversion for the temporal evolution of the seafloor vertical deformation combined with the  
 182 theory for ocean-bottom pressure inside the focal area described in section 2.1. We represent the  
 183 vertical displacement at the seafloor ( $u_z(x, y, t)$ ) by the superposition of basis functions,

184

$$185 \quad u_z(x, y, t) = \sum_{i=1}^{N_x} \sum_{j=1}^{N_y} \sum_{k=1}^{N_t} m_{ijk} U_{z,ij}(x, y) \tau_k(t). \quad (5)$$

186

187 The basis function for the spatial distribution of the seafloor vertical displacement  $U_{z,ij}(x, y)$  is  
 188 given by

189

$$190 \quad U_{z,ij}(x, y) = \left[ \frac{1}{2} + \frac{1}{2} \cos\left(\frac{2\pi(x-x_i)}{L_x}\right) \right] \left[ \frac{1}{2} + \frac{1}{2} \cos\left(\frac{2\pi(y-y_j)}{L_y}\right) \right]$$

$$191 \quad \text{for } x_i - \frac{L_x}{2} \leq x \leq x_i + \frac{L_x}{2}, y_j - \frac{L_y}{2} \leq y \leq y_j + \frac{L_y}{2}, \quad (6)$$

192

193 which takes the maximum value at  $(x_i, y_j)$ . The displacement time function  $\tau_k(t)$  is given by

194

$$195 \quad \tau_k(t) = \begin{cases} 0 & \text{for } t \leq t_k \\ \frac{1}{T_d} \left[ t - \frac{T_d}{2\pi} \sin\left(\frac{2\pi(t-t_k)}{T_d}\right) \right] & \text{for } t_k \leq t \leq t_k + T_d, \\ 1 & \text{for } t_k + T_d \leq t \end{cases} \quad (7)$$

196

197 where the function begins to increase at  $t = t_k$  and reaches 1 after the duration  $T_d$ . The  
 198 coefficient  $m_{ijk}$  in Eq. (5) represents the displacement amplitude of the  $(i, j, k)$ -th function  
 199  $U_{z,ij}(x, y) \tau_k(t)$ .

200 The hydrostatic pressure change at the  $n$ -th OBP located at  $(x_n, y_n)$  is given by

201

$$202 \quad p_{\text{hydrostatic}}(x_n, y_n, t) = \rho_0 g_0 [\eta(x_n, y_n, t) - u_z(x_n, y_n, t)]. \quad (8)$$

203

204 The first and second terms represent the pressure changes due to the tsunami and the vertical  
 205 displacement at the seafloor at  $(x_n, y_n)$ , respectively. The tsunami height  $\eta(x, y, t)$  is  
 206 numerically calculated by solving the linear tsunami equation from the seafloor vertical

207 displacement  $u_z(x, y, t)$  (Eq. (5)). Since the  $p_{\text{hydrostatic}}(x_n, y_n, t)$  is linear with respect to the  
 208 seafloor displacement, we represent Eq. (9) as the superposition using  $m_{ijk}$ :

$$209 \quad p_{\text{hydrostatic}}(x_n, y_n, t) = \sum_{i=1}^{N_x} \sum_{j=1}^{N_y} \sum_{k=1}^{N_t} m_{ijk} G_{ijk,n}^{\text{hydrostatic}}(x_n, y_n, t). \quad (10)$$

211  
 212 We refer to  $G_{ijk,n}^{\text{hydrostatic}}(x, y, t)$  as the hydrostatic pressure Green's function in this study, which  
 213 is the hydrostatic pressure change at  $(x, y)$  excited by the unit vertical displacement of  
 214  $U_{z,ij}(x, y)\tau_k(t)$ .

215 The dynamic pressure change at the  $n$ -th OBP located at  $(x_n, y_n)$  (Eq. (3)) is given by  
 216 the displacement of Eq. (5):

$$217 \quad p_{\text{dynamic}}(x_n, y_n, t) = \rho_0 h_0 \frac{\partial^2 u_z(x_n, y_n, t)}{\partial t^2}$$

$$218 \quad = \rho_0 h_0 \sum_{i=1}^{N_x} \sum_{j=1}^{N_y} \sum_{k=1}^{N_t} m_{ijk} U_{z,ij}(x_n, y_n) \frac{\partial^2 \tau_k(t)}{\partial t^2}$$

$$219 \quad = \sum_{i=1}^{N_x} \sum_{j=1}^{N_y} \sum_{k=1}^{N_t} m_{ijk} G_{ijk,n}^{\text{dynamic}}(x_n, y_n, t), \quad (11)$$

220  
 221 where

$$222 \quad \frac{\partial^2 \tau_k(t)}{\partial t^2} = \begin{cases} 0 & \text{for } t \leq t_k, t_k + T_d \leq t \\ \frac{2\pi}{T_d^2} \sin\left(\frac{2\pi(t-t_k)}{T_d}\right) & \text{for } t_k \leq t \leq t_k + T_d \end{cases} \quad (12)$$

223  
 224 We refer to  $G_{ijk,n}^{\text{dynamic}}(x, y, t)$  as the dynamic pressure Green's function, which represents the  
 225 dynamic pressure change at  $(x, y)$  excited by the unit vertical displacement of  $U_{z,ij}(x, y)\tau_k(t)$ .

226 By using Eqs. (10) and (11), we represent the pressure change at the  $n$ -th OBP excited by  
 227 the vertical seafloor motions as

$$228 \quad p(x_n, y_n, t) = \sum_{i=1}^{N_x} \sum_{j=1}^{N_y} \sum_{k=1}^{N_t} m_{ijk} \left[ G_{ijk,n}^{\text{hydrostatic}}(x_n, y_n, t) + G_{ijk,n}^{\text{dynamic}}(x_n, y_n, t) \right]$$

$$229 \quad = \sum_{i=1}^{N_x} \sum_{j=1}^{N_y} \sum_{k=1}^{N_t} m_{ijk} G_{ijk}(x_n, y_n, t), \quad (13)$$

230  
 231 where the Green's function  $G_{ijk}(x, y, t)$  is given by

$$232 \quad G_{ijk}(x, y, t) = G_{ijk}^{\text{hydrostatic}}(x, y, t) + G_{ijk}^{\text{dynamic}}(x, y, t), \quad (14)$$

233  
 234 which represents the pressure change at  $(x, y)$  excited by the unit vertical displacement of  
 235  $U_{z,ij}(x, y)\tau_k(t)$ .

240 We estimate the displacement amplitude  $m_{ijk}$  as model parameters in a linear inversion  
 241 problem given by Eq. (13), where the pressure change at the  $n$ -th OBP is used as the data. Using  
 242 the estimated  $m_{ijk}$  with Eqs. (10) and (11), the observed pressure change at the  $n$ -th OBP can be  
 243 decomposed into the hydrostatic and dynamic components. The time history of the vertical  
 244 acceleration can also be extracted using Eq. (11), as

$$245 \frac{\partial^2 u_z(x_n, y_n, t)}{\partial t^2} = \frac{1}{\rho_0 h_0} \sum_{i=1}^{N_x} \sum_{j=1}^{N_y} \sum_{k=1}^{N_t} m_{ijk} G_{ijk,n}^{\text{dynamic}}(x_n, y_n, t)$$

$$246 = \sum_{i=1}^{N_x} \sum_{j=1}^{N_y} \sum_{k=1}^{N_t} m_{ijk} U_{z,ij}(x_n, y_n) \frac{\partial^2 \tau_k(t)}{\partial t^2}. \quad (15)$$

247  
 248 In the same manner, vertical velocity and displacement can also be obtained. For example,  
 249 vertical velocity is expressed as

$$250 \frac{\partial u_z(x_n, y_n, t)}{\partial t} = \sum_{i=1}^{N_x} \sum_{j=1}^{N_y} \sum_{k=1}^{N_t} m_{ijk} U_{z,ij}(x_n, y_n) \frac{\partial \tau_k(t)}{\partial t} \quad (16)$$

251 where

$$252 \frac{\partial \tau_k(t)}{\partial t} = \begin{cases} 0 & \text{for } t \leq t_k, t_k + T_d \leq t \\ \frac{1}{T_d} \left[ 1 - \cos\left(\frac{2\pi(t-t_k)}{T_d}\right) \right] & \text{for } t_k \leq t \leq t_k + T_d \end{cases} \quad (17)$$

253 To calculate the Green's function, we suppose the  $x$ - and  $y$ -directions are along the  
 254 trench-normal and trench-parallel directions, respectively. We distribute the spatial basis  
 255 function  $U_{z,ij}$  in an area of 220 km  $\times$  270 km (gray dots in Figure 1a). We suppose the elliptical-  
 256 shaped unit sources to be  $L_x = 20$  km and  $L_y = 30$  km, and that each of them overlaps with  
 257 their adjacent ones at horizontal intervals of  $\Delta x = L_x/2$  and  $\Delta y = L_y/2$  (inset of Figure 1a). We  
 258 also distribute the temporal basis function  $\tau_k$  during the first 120 s from the origin time (inset of  
 259 Figure 1a). Duration of the displacement is assumed as  $T_d = 10$  s and the temporal interval is set  
 260 as  $\Delta t = T_d/2 = 5$  s. To calculate the hydrostatic Green's function, tsunami height is numerically  
 261 simulated from the initial tsunami height distribution using the linear dispersive tsunami equation  
 262 (e.g., Saito, 2019) with a time step interval of 1 s. We use the bathymetry data of GEBCO  
 263 Bathymetric Compilation Group (2020), decimating to a spatial grid interval of 2 km. The input  
 264 sea-surface height for the tsunami calculation is calculated from the unit seafloor displacement  
 265  $U_{z,ij}(x, y)$  with the water wave theory assuming a constant depth of 6 km (Kajiura, 1963). The  
 266 dynamic Green's functions are also calculated, using the seawater depth  $h_0$  for each station  
 267 (Table S1). After the calculation of the Green's functions, the same filter as applied to the  
 268 observation is also applied to the Green's functions.

269 In the inversion, we impose the constraints of the spatial smoothing (Baba et al., 2006)  
 270 and spatial damping. The weights of each constraint are determined based on trial and error. The  
 271  
 272

275 deformations are allowed to begin at  $t = 0$  s. We use 3600-s time windows for the OBPs of  
276 Tohoku University and 1800-s for the OBPs of ERI for the inversion.

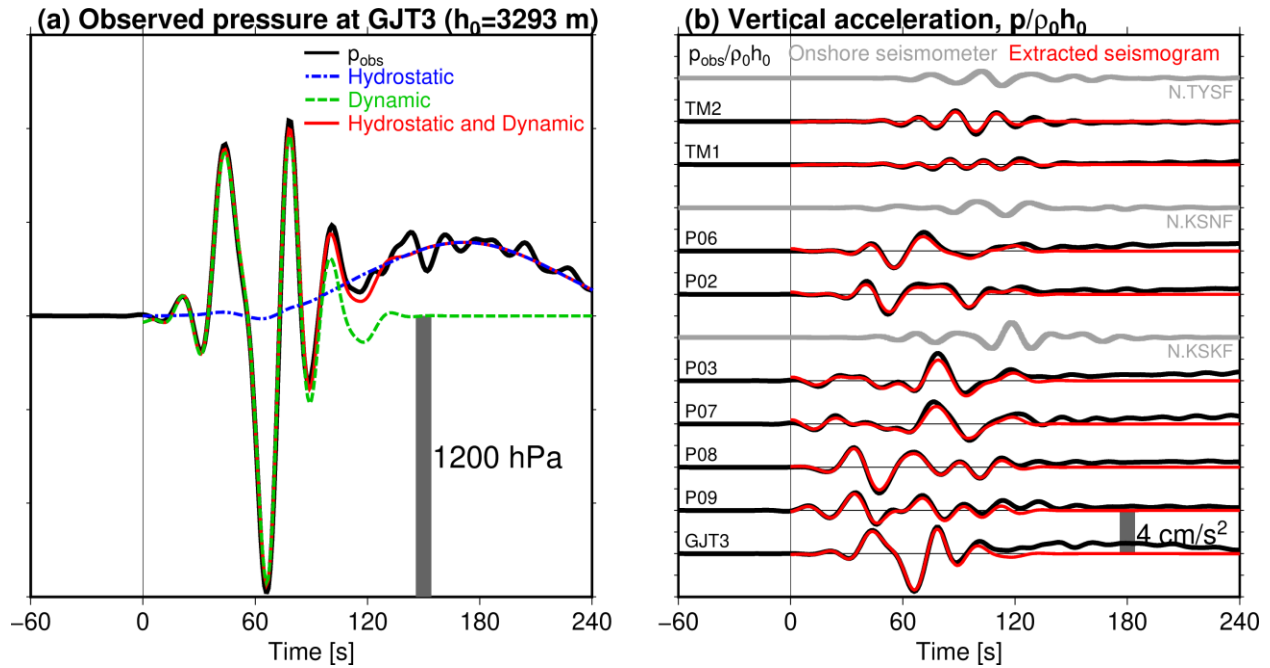
277

### 278 **3 Results**

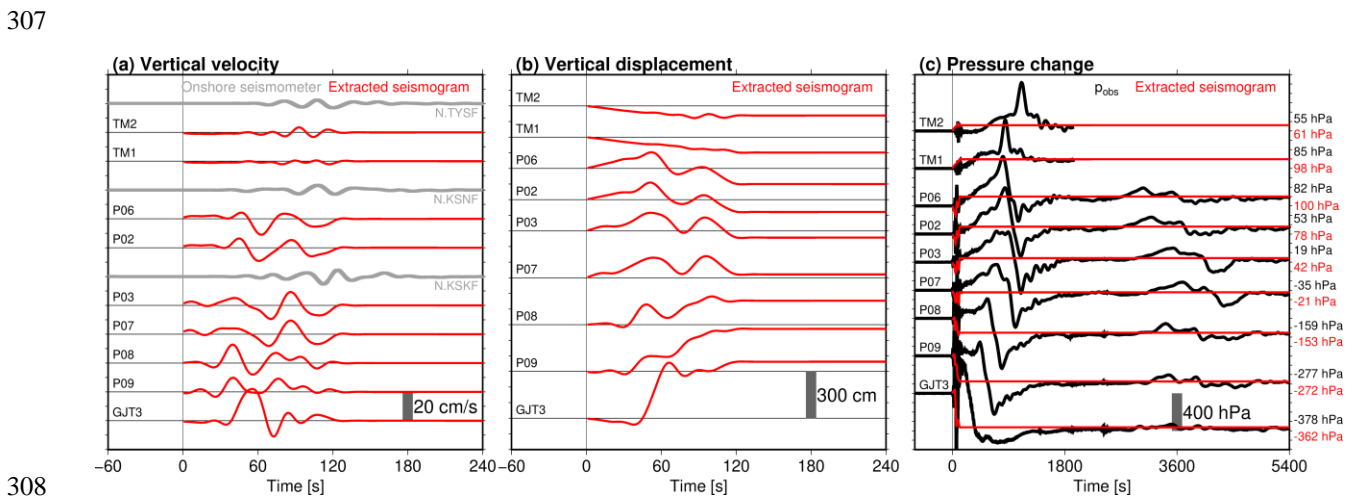
279 In Figure 2a, we compare the observed pressure changes at GJT3 with the synthesized  
280 ones (see Figure S1 for the other OBPs). Figure 2b shows the extracted vertical accelerograms at  
281 the OBPs using the estimated model parameter  $m_{ijk}$  in Eq. (12). Compared to the observed  
282 pressure changes divided by  $\rho_0 h_0$  (black traces), the extracted accelerograms (red traces) do not  
283 contain the low-frequency pressure signals due to the tsunami, which are evident after  $\sim 120$  s  
284 from the origin time. High-frequency pressure changes for the first 120 s are explained by the  
285 dynamic pressure components (green trace in Figure 2a) and the subsequent low-frequency  
286 pressure changes are modeled by the hydrostatic components (blue trace), and the overall  
287 pressure changes were explained very well by both pressure changes (red trace). From the  
288 amplitude spectra of the pressure change at GJT3 in Figure S2, we confirm that the calculated  
289 hydrostatic and dynamic pressure changes are dominant only in the low- and high-frequency  
290 ranges, respectively. In Figure 2b, we also plot the accelerograms of the onshore broadband  
291 strong-motion seismometer from the F-net (Okada et al., 2004, black triangles in Figure 1a) by  
292 gray traces. Although the arrivals of the main wave packet are delayed, the onshore seismograms  
293 are similar to the extracted ocean-bottom seismograms at the OBPs near each station (compare  
294 N.TYSF with TM1 and TM2, N.KSNF with P02 and P06, and N.KSKF with P03 and P07). We  
295 also show the vertical velocity and displacement waveforms in Figures 3a and 3b, respectively.  
296 The amounts of the calculated vertical displacements are surprisingly consistent with the  
297 observed pressure offset changes due to the permanent deformation (Figure 3c). These  
298 comparisons indicate the validity of the extracted seafloor vertical seismograms.

299

300



301  
 302 **Figure 2.** (a) Comparison of the observed OBP waveform (black) at GJT3 and the synthesized  
 303 ones (blue: hydrostatic, green: dynamic, and red: both pressure changes). (b) Extracted vertical  
 304 accelerograms at the OBPs (red traces). Observed pressure changes divided by  $\rho_0 h_0$ , which  
 305 includes both tsunamis and dynamic pressure change components, are also shown by black traces.  
 306 Gray traces are the observed accelerograms at the onshore seismometers.



308  
 309 **Figure 3.** Time series of the extracted vertical seismograms from the OBPs (red traces), for (a)  
 310 velocity and (b) displacement. Gray traces are the observed seismograms at the onshore  
 311 seismometers. (c) Comparison of the observed pressure time series (black) and those expected  
 312 from the extracted displacement (red). The final pressure offsets, calculated by averaging the last  
 313 600 s time window, are also shown.

314

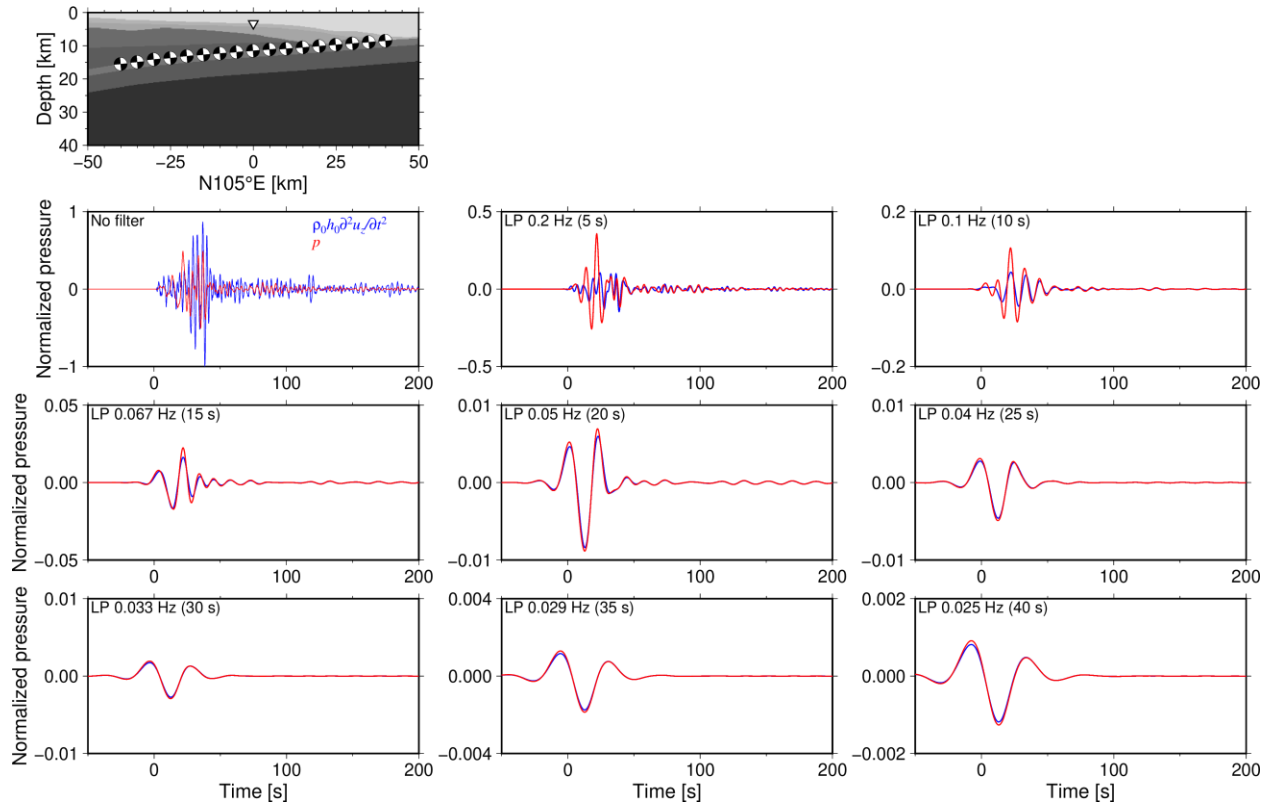
315 It is worth pointing out that the near-field seismograms inside the tsunami source where  
316 the vertical displacement was extremely large during the Tohoku-Oki earthquake had never been  
317 reported previously. In the accelerograms at the OBPs inside the main rupture area (GJT3, P08,  
318 and P09), two dominant positive pulses are confirmed (Figure 2b). The duration of the second  
319 pulse at GJT3 is relatively short compared to the first one, whereas the durations in both pulses at  
320 P08 and P09 are similar. From the velocity seismogram at GJT3, located ~50 km landward from  
321 the trench axis, only one peak with a relatively long duration is confirmed (Figure 3a). On the  
322 other hand, at P08 and P09, located near the epicenter and ~100 km from the trench axis, there  
323 are two velocity peaks at  $t \sim 40$  and  $\sim 70$  s (Figure 3a). These characteristics may reflect the  
324 rupture kinematics of the mainshock. One possible interpretation is that the rupture, or energy  
325 release, at the fault beneath P08 and P09, which are located near the epicenter, occurred twice.  
326 This feature is also suggested by the kinematic modeling of the mainshock from the regional or  
327 global seismograms (Lay, 2018).

328

#### 329 4. Discussions

330 This study used a lowpass filter with a cutoff of 0.05 Hz to satisfy the condition that the  
331 seawater is considered as incompressible fluid. However, if the contribution of the seawater  
332 elasticity cannot be neglected in this frequency range, the extracted seafloor seismogram may be  
333 incorrect. To confirm validity of the extracted seismograms at  $f < 0.05$  Hz, we conduct a  
334 numerical simulation of the two-dimensional P-SV seismic wave propagation using the finite  
335 difference method (Maeda et al., 2017, Figure 4). We assume the vertical cross-section passing  
336 through GJT3 along the trench-normal direction (azimuth =  $105^\circ$ ) from the extended Japan  
337 Integrated Velocity Structure Model (Koketsu et al., 2012) with a grid interval of 0.2 km (top  
338 panel in Figure 4). We distribute point sources along the plate boundary. We assume their  
339 rupture begins at the same time and the source durations are 4 s. We apply lowpass filters with  
340 different cutoffs to compare the pressure ( $p = -\sigma_{zz}$ , red traces) and the pressure-converted  
341 vertical acceleration ( $\rho_0 h_0 d^2 u_z / dt^2$ , blue traces) at the station GJT3. As a result, when the  
342 waveforms include high-frequency components of  $f > \sim 0.1$  Hz, the two waveforms are different  
343 from each other. When only focusing on the lower frequency ranges, less than 0.05 Hz, the two  
344 waveforms agree with each other. Based on this simulation, we conclude that Eq. (3) holds in the  
345 frequency range of  $f < 0.05$  Hz, and our extracted seismograms are valid.

346



347

348 **Figure 4.** Result of the two-dimensional simulation of the seismic wave propagation. Structure  
 349 model, point source location, and station location are shown in the top panel, and bottom panels  
 350 show comparisons of the pressure-converted vertical accelerogram (blue) and the pressure  
 351 waveform (red) in which lowpass filters with different cutoffs are applied.

352

353

354

355 This study adopted the inversion-based method to extract the ground motion signals  
 356 from the OBP data. However, one might think that the bandpass filters are also capable of  
 357 extracting the seismograms by removing the low-frequency hydrostatic components. In order to  
 358 evaluate this, we investigate the accelerograms calculated based on a bandpass filter with  
 359 passbands of 0.01–0.05 Hz, shown in Figure S3a (black dashed line traces). The bandpass  
 360 filtered accelerograms seem to agree with those extracted by our approach. However, the  
 361 waveforms do not agree at all when integrating to the displacement (Figure S3b). This is because  
 362 the permanent offsets are removed by the bandpass filter. Considering a slow rupture near a  
 363 trench as in a tsunami earthquake (e.g., Lay et al., 2012), the megathrust earthquake rupture  
 364 process possibly spans broadband frequency ranges. Because the spectral components of the  
 365 mainshock ground motions possibly range into the low-frequency tsunami-dominant spectral  
 366 bands, we must not use a highpass filter, which reduces the low-frequency components. It is  
 367 essential to use a lowpass filter and to employ an inversion-based method with the tsunami

368 generation theory to appropriately extract the broadband vertical ground motion including the  
369 low-frequency permanent offset component.

370 We could extract near-field seismograms from the OBP data to discuss the source  
371 kinematics of the mainshock. This could never be achieved in the past when no OBP was  
372 installed inside the focal area and the tsunami generation theory was not established. By  
373 combining near-field OBP observation and the tsunami generation theory, it is expected that the  
374 parameters for the rupture kinematics and dynamics can be constrained more precisely,  
375 particularly for the subduction zone (e.g., Ide & Takeo, 1997; Kozdon & Dunham, 2014; Ma &  
376 Nie, 2019). In addition, developments in deep-ocean OBP observation enable us to capture the  
377 higher-frequency ocean-acoustic wave signals up to ~1 Hz (Webb & Nooner, 2016; Heidarzadeh  
378 & Gusman, 2018; Kubota et al., 2020, Figure 1), which can be modeled by numerical simulation  
379 considering the seawater as the elastic body (Figure 4, Maeda et al., 2017; Saito et al., 2019). In  
380 deep-ocean measurements, it is still hard to control the installation environment and some studies  
381 have reported that the near-field OBS rotated due to strong shaking on the seafloor (Nakamura &  
382 Hayashimoto, 2018; Takagi et al., 2019). In such a situation, the near-field OBPs must produce  
383 powerful datasets to constrain the earthquake source information. Taking these facts into account,  
384 the high-frequency near-field OBP data should be more utilized to deepen our geophysical  
385 understanding of the subduction zone, as widely as the data from onshore and offshore seismic  
386 instruments.

387 Our approach utilizing dynamic pressure may also be applicable to practical real-time  
388 tsunami early warnings (e.g., Melger & Hayes, 2019; Tsushima et al., 2011; 2012). Inside the  
389 focal area, the OBPs observe no hydrostatic pressure changes just after the origin time, because  
390 the sea-surface height change and seafloor vertical displacement are almost equivalent soon after  
391 the earthquake occurrence (Tsushima et al., 2012). If we utilize the dynamic pressure changes as  
392 vertical motion signals, which are dominant in the first few minutes, the accuracy of the tsunami  
393 forecast immediately after the earthquake rupture starts will be improved. This study showed the  
394 future potential of the high-frequency pressure changes recorded by the OBPs.

395

#### 396 **4 Conclusion**

397 We developed a method to extract near-field seismograms from the OBP data from  
398 inside the focal area. We applied the method to the near-field OBP data of the 2011 Tohoku-Oki  
399 earthquake to extract the ground motions inside the focal area, whereas the near-field  
400 seismograms during the Tohoku-Oki earthquake have never been reported yet. Our analysis  
401 successfully decomposed the observed OBP data into the dynamic pressure changes dominant in  
402 the first ~120 s and the subsequent hydrostatic pressure changes due to tsunamis and permanent  
403 seafloor deformation. The extracted seismograms suggested that two dominant energy releases  
404 occurred beneath the OBPs near the epicenter. We confirmed the validity of the extracted  
405 seismograms based on the numerical seismic wave propagation simulation. Because the  
406 bandpass filter to reduce the low-frequency hydrostatic components also reduces the low-

407 frequency ground motion components, our inversion-based method is essential to appropriately  
408 extract the ground motion waveform including the low-frequency permanent offset components.  
409 The high-frequency pressure change signals in the near-field OBP should be utilized more  
410 widely, for geophysical research as well as real-time tsunami forecasting.

411

## 412 **Data Availability Statement**

413 The OBP data off Miyagi installed by Tohoku University are available in Data Set S1 (during the  
414 review process. The file will be uploaded on the online repository after the acceptance). The  
415 OBP data off Kamaishi were provided upon request to ERI. The bathymetry data of GEBCO  
416 2020 Grid (GEBCO Bathymetric Compilation Group 2020, 2020) are available at  
417 [https://www.gebco.net/data\\_and\\_products/gridded\\_bathymetry\\_data/](https://www.gebco.net/data_and_products/gridded_bathymetry_data/). The F-net onshore  
418 seismometer data are available at <http://doi.org/10.17598/nied.0005>. The numerical simulation of  
419 the P-SV seismic wave propagation was conducted by using OpenSWPC (Maeda et al., 2017)  
420 Version 5.0.2, available at <https://doi.org/10.5281/zenodo.3712650>. We used Seismic Analysis  
421 Code (SAC) software for data processing (Goldstein et al., 2003). Figures were prepared using  
422 Generic Mapping Tools Version 6 (GMT6) software (Wessel et al., 2019).

423

## 424 **Acknowledgments**

425 This study was financially supported by the research project “Research concerning  
426 Interaction between the Tokai, Tonankai, and Nankai Earthquakes” of Ministry of Education,  
427 Culture, Sports, Science and Technology (MEXT), Japan, and by Japan Society for the  
428 Promotion of Science (JSPS) KAKENHI Grant Numbers JP20244070, JP26000002,  
429 JP15K17752, JP19H00708, JP19H02409, 19H05596, JP19K04021, and JP19K14818. TK thanks  
430 Yoshihiro Ito of Kyoto University for fruitful comments. TK also thanks Naotaka Y. Chikasada,  
431 Hisahiko Kubo, and Osamu Sandanbata of National Research Institute for Earth Science and  
432 Disaster Resilience for insightful discussions. The installation and retrieval of the OBPs of  
433 Tohoku University were conducted via Research Vessel (*R/V Keifu-maru* and *R/V Ryofu-maru*  
434 (Japan Meteorological Agency), Supply Vessels (*S/Vs Kaiko* and *Kaiyu* (Offshore Operation  
435 Co., Ltd.) and *S/V Shinsei-maru* (Fukada Salvage Co., Ltd). The OBPs at P03, P07, P08, and P09  
436 were recovered in September 2011 by using Remotely Operated Vehicle (ROV) *Hakuyo-3000*  
437 (Fukada Salvage Co., Ltd.) (Hino et al., 2012; Arai et al., 2013). TK also thanks the captains and  
438 crews of these vessels and the staff and technicians at ERI for their efforts for their operation.

439

440 **References**

- 441 Aki, K. & Richards, P. G. (2002). *Quantitative seismology* (2nd ed.). Mill Valley, CA:  
442 University Science Books.
- 443 An, C., Cai, C., Zheng, Y., Meng, L., & Liu, P. (2017). Theoretical solution and applications of  
444 ocean bottom pressure induced by seismic seafloor motion. *Geophysical Research*  
445 *Letters*, *44*, 10272–10281. <https://doi.org/10.1002/2017GL075137>
- 446 Arai, K., Naruse, H., Miura, R., Kawamura, K., Hino, R., Ito, Y., Inazu, D., Yokokawa, M.,  
447 Izumi, N., Murayama, M., & Kasaya, T. (2013). Tsunami-generated turbidity current  
448 of the 2011 Tohoku-Oki earthquake. *Geology*, *41*(11), 1195–1198.  
449 <https://doi.org/10.1130/G34777.1>
- 450 Baba, T., Hirata, K., Hori, T., & Sakaguchi, H. (2006). Offshore geodetic data conducive to the  
451 estimation of the afterslip distribution following the 2003 Tokachi-oki earthquake.  
452 *Earth and Planetary Science Letters*, *241*, 281–292.  
453 <https://doi.org/10.1016/j.epsl.2005.10.019>
- 454 Baba, T., Takahashi, N., Kaneda, Y., Ando, K., Matsuoka, D., & Kato, T. (2015). Parallel  
455 implementation of dispersive tsunami wave modeling with a nesting algorithm for the  
456 2011 Tohoku tsunami. *Pure and Applied Geophysics*, *172*, 3455–3472.  
457 <https://doi.org/10.1007/s00024-015-1049-2>
- 458 Dettmer, J., Hawkins, R., Cummins, P. R., Hossen, J., Sambridge, M., Hino, R., & Inazu, D.  
459 (2016). Tsunami source uncertainty estimation : The 2011 Japan tsunami. *Journal of*  
460 *Geophysical Research: Solid Earth*, *121*, 4483–4505.  
461 <https://doi.org/10.1002/2015JB012764>
- 462 Filloux, J. H. (1982). Tsunami recorded on the open ocean floor. *Geophysical Research Letters*,  
463 *9*, 25–28. <https://doi.org/10.1029/GL009I001P00025>
- 464 Fujiwara, T., Kodaira, S., No, T., Kaiho, Y., Takahashi, N., & Kaneda, Y. (2011). The 2011  
465 Tohoku-Oki earthquake: Displacement reaching the trench axis. *Science*, *334*, 1240.  
466 <https://doi.org/10.1126/science.1211554>
- 467 Fujiwara, T., dos Santos Ferreira, C., Bachmann, A. K., Strasser, M., Wefer, G., Sun, T., ...  
468 Kodaira, S. (2017). Seafloor displacement after the 2011 Tohoku-oki earthquake in the  
469 northern Japan Trench examined by repeated bathymetric surveys. *Geophysical*  
470 *Research Letters*, *44*, 11,833-11,839. <https://doi.org/10.1002/2017GL075839>
- 471 Fukuyama, E., & Mikumo, T. (2007). Slip-weakening distance estimated at near-fault stations.  
472 *Geophysical Research Letters*, *34*, L09302. <https://doi.org/10.1029/2006GL029203>
- 473 Fukuyama, E., & Suzuki, W. (2016). Near-fault deformation and  $D_c$  during the 2016 Mw7.1  
474 Kumamoto earthquake. *Earth, Planets and Space*, *68*, 194.  
475 <https://doi.org/10.1186/s40623-016-0570-6>

- 476 GEBCO Bathymetric Compilation Group 2020 (2020). *GEBCO 2020 Grid—a continuous terrain*  
477 *model of the global oceans and land* [Data set]. British Oceanographic Data Centre,  
478 National Oceanography Centre, Natural Environment Research Council, United  
479 Kingdom. <https://doi.org/10/dtg3>
- 480 Goldstein, P., Dodge, D., Firpo, M., & Minner L. (2003). SAC2000: Signal processing and  
481 analysis tools for seismologists and engineers. In: W. H. K. Lee, H. Kanamori, P. C.  
482 Jennings, & C. Kisslinger (Eds.), *International Handbook of Earthquake and*  
483 *Engineering Seismology* (Vol. 81(B), pp. 1613–1614). London: Academic Press.  
484 [https://doi.org/10.1016/S0074-6142\(03\)80284-X](https://doi.org/10.1016/S0074-6142(03)80284-X)
- 485 Gusman, A. R., Tanioka, Y., Sakai, S., & Tsushima, H. (2012). Source model of the great 2011  
486 Tohoku earthquake estimated from tsunami waveforms and crustal deformation data.  
487 *Earth and Planetary Science Letters*, 341–344, 234–242.  
488 <https://doi.org/10.1016/j.epsl.2012.06.006>
- 489 Heidarzadeh, M. & Gusman A. R. (2018). Application of dense offshore tsunami observations  
490 from ocean bottom pressure gauges (OBPGs) for tsunami research and early warnings.  
491 In Durrani T., Wang W., Forbes S. (Eds.), *Geological Disaster Monitoring Based on*  
492 *Sensor Networks* (pp. 7-22). Singapore: Springer Singapore.  
493 [https://doi.org/10.1007/978-981-13-0992-2\\_2](https://doi.org/10.1007/978-981-13-0992-2_2)
- 494 Hino, R. (2015). An overview of the Mw 9, 11 March 2011, Tohoku earthquake. *Summary of the*  
495 *Bulletin of the International Seismological Centre*, 48, 100–132.  
496 <https://doi.org/10.5281/zenodo.998789>
- 497 Hino, R., Suzuki, S., Kubota, T., Ito, Y., & Fujimoto, H. (2012). Video image of seafloor near  
498 the epicenter of the 2011 Great Tohoku Earthquake. Abstract SSS39-P05 presented at  
499 JpGU Meeting 2012, Makuhari, Japan, May20–25, 2012. Retrieved October 15, 2020,  
500 from [http://www2.jpгу.org/meeting/2012/session/PDF/S-SS39/SSS39-P05\\_e.pdf](http://www2.jpгу.org/meeting/2012/session/PDF/S-SS39/SSS39-P05_e.pdf)
- 501 Hino, R., Inazu, D., Ohta, Y., Ito, Y., Suzuki, S., Iinuma, T., ... Kaneda, Y. (2014). Was the  
502 2011 Tohoku-Oki earthquake preceded by aseismic preslip? Examination of seafloor  
503 vertical deformation data near the epicenter. *Marine Geophysical Research*, 35, 181–  
504 190. <https://doi.org/10.1007/s11001-013-9208-2>
- 505 Hossen, M. J., Cummins, P. R., Dettmer, J., & Baba, T. (2015). Tsunami waveform inversion for  
506 sea surface displacement following the 2011 Tohoku earthquake: Importance of  
507 dispersion and source kinematics. *Journal of Geophysical Research: Solid Earth*, 120,  
508 6452–6473. <https://doi.org/10.1002/2015JB011942>
- 509 Ide, S., & Takeo, M. (1997). Determination of constitutive relations of fault slip based on  
510 seismic wave analysis. *Journal of Geophysical Research*, 102(B12), 27,379–27,391.  
511 <https://doi.org/10.1029/97JB02675>

- 512 Iinuma, T., Hino, R., Kido, M., Inazu, D., Osada, Y., Ito, Y., ... Miura, S. (2012). Coseismic slip  
 513 distribution of the 2011 off the Pacific Coast of Tohoku Earthquake (M9.0) refined by  
 514 means of seafloor geodetic data. *Journal of Geophysical Research*, *117*, B07409.  
 515 <https://doi.org/10.1029/2012JB009186>
- 516 Ito, Y., Tsuji, T., Osada, Y., Kido, M., Inazu, D., Hayashi, Y., ... Fujimoto, H. (2011). Frontal  
 517 wedge deformation near the source region of the 2011 Tohoku-Oki earthquake.  
 518 *Geophysical Research Letters*, *38*(15), L00G05.  
 519 <https://doi.org/10.1029/2011GL048355>
- 520 Ito, Y., Webb, S. C., Kaneko, Y., Wallace, L. M., & Hino, R. (2020). Sea surface gravity waves  
 521 excited by dynamic ground motions from large regional earthquakes. *Seismological*  
 522 *Research Letters*. <https://doi.org/10.1785/0220190267>
- 523 Kajiura, K. (1963). The leading wave of a tsunami. *Bulletin of the Earthquake Research*  
 524 *Institute*, *41*, 535–571.
- 525 Kanazawa, T., & Hasegawa, A. (1997). Ocean-bottom observatory for earthquakes and tsunami  
 526 off Sanriku, north-eastern Japan using submarine cable. *Proceedings of International*  
 527 *Workshop on Scientific Use of Submarine Cables*, 208–209.
- 528 Kaneko, Y., Fukuyama, E., & Hamling, I. J. (2017). Slip-weakening distance and energy budget  
 529 inferred from near-fault ground deformation during the 2016 Mw7.8 Kaikōura  
 530 earthquake. *Geophysical Research Letters*, *44*, 4765–4773.  
 531 <https://doi.org/10.1002/2017GL073681>
- 532 Kido, M., Osada, Y., Fujimoto, H., Hino, R., & Ito, Y. (2011). Trench-normal variation in  
 533 observed seafloor displacements associated with the 2011 Tohoku-Oki earthquake.  
 534 *Geophysical Research Letters*, *38*, L24303. <https://doi.org/10.1029/2011GL050057>
- 535 Kodaira, S., Fujiwara, T., Fujie, G., Nakamura, Y., & Kanamatsu, T. (2020). Large coseismic  
 536 slip to the trench during the 2011 Tohoku-Oki earthquake. *Annual Review of Earth*  
 537 *and Planetary Sciences*, *48*, 321–343. [https://doi.org/10.1146/annurev-earth-071719-](https://doi.org/10.1146/annurev-earth-071719-055216)  
 538 [055216](https://doi.org/10.1146/annurev-earth-071719-055216)
- 539 Koketsu, K., Miyake, H., Suzuki, H. (2012). Japan integrated velocity structure model version 1.  
 540 In: Proceedings of the 15th world conference on earthquake engineering. Lisbon,  
 541 Portugal, 24–28 September. Retrieved October 15, 2020, from  
 542 [https://www.iitk.ac.in/nicee/wcee/article/WCEE2012\\_1773.pdf](https://www.iitk.ac.in/nicee/wcee/article/WCEE2012_1773.pdf)
- 543 Kozdon, J. E., & Dunham, E. M. (2014). Constraining shallow slip and tsunami excitation in  
 544 megathrust ruptures using seismic and ocean acoustic waves recorded on ocean-  
 545 bottom sensor networks. *Earth and Planetary Science Letters*, *396*, 56–65.  
 546 <https://doi.org/10.1016/j.epsl.2014.04.001>
- 547 Kubota, T., Hino, R., Inazu, D., Ito, Y., Iinuma, T., Ohta, Y., ... Suzuki, K. (2017). Coseismic  
 548 slip model of offshore moderate interplate earthquakes on March 9, 2011 in Tohoku

- 549 using tsunami waveforms. *Earth and Planetary Science Letters*, 458, 241–251.  
550 <https://doi.org/10.1016/j.epsl.2016.10.047>
- 551 Kubota, T., Saito, T., Suzuki, W., & Hino, R. (2017). Estimation of seismic centroid moment  
552 tensor using ocean bottom pressure gauges as seismometers. *Geophysical Research*  
553 *Letters*, 44, 10907–10915. <https://doi.org/10.1002/2017GL075386>
- 554 Kubota, T., Saito, T., Ito, Y., Kaneko, Y., Wallace, L. M., Suzuki, S., ... Henrys, S. (2018).  
555 Using tsunami waves reflected at the coast to improve offshore earthquake source  
556 parameters: application to the 2016 Mw 7.1 Te Araroa earthquake, New Zealand.  
557 *Journal of Geophysical Research: Solid Earth*, 123, 8767–8779.  
558 <https://doi.org/10.1029/2018JB015832>
- 559 Kubota, T., Saito, T., Chikasada, N. Y. & Suzuki, W. (2020). Ultra-broadband seismic and  
560 tsunami wave observation of high-sampling ocean-bottom pressure gauge covering  
561 periods from seconds to hours. *Earth and Space Science*, 7, e2020EA001197.  
562 <https://doi.org/10.1029/2020EA001197>
- 563 Lay, T. (2018). A review of the rupture characteristics of the 2011 Tohoku-oki Mw 9.1  
564 earthquake. *Tectonophysics*, 733, 4–36. <https://doi.org/10.1016/j.tecto.2017.09.022>
- 565 Lay, T., Ammon, C. J., Kanamori, H., Xue, L., & Kim, M. J. (2011). Possible large near-trench  
566 slip during the 2011 Mw 9.0 off the Pacific coast of Tohoku Earthquake. *Earth,*  
567 *Planets and Space*, 63, 687–692. <https://doi.org/10.5047/eps.2011.05.033>
- 568 Lay, T., Kanamori, H., Ammon, C. J., Koper, K. D., Hutko, A. R., Ye, L., ... Rushing, T. M.  
569 (2012). Depth-varying rupture properties of subduction zone megathrust faults.  
570 *Journal of Geophysical Research*, 117, B04311.  
571 <https://doi.org/10.1029/2011JB009133>
- 572 Ma, S., & Nie, S. (2019). Dynamic wedge failure and along-arc variations of tsunamigenesis in  
573 the Japan Trench margin. *Geophysical Research Letters*, 46, 8782–8790.  
574 <https://doi.org/10.1029/2019GL083148>
- 575 Madariaga, R., Ruiz, S., Rivera, E., Leyton, F., & Baez, J. C. (2019). Near-field spectra of large  
576 earthquakes. *Pure and Applied Geophysics*, 176, 983–1001.  
577 <https://doi.org/10.1007/s00024-018-1983-x>
- 578 Maeda, T., Furumura, T., Sakai, S., & Shinohara, M. (2011). Significant tsunami observed at  
579 ocean-bottom pressure gauges during the 2011 off the Pacific coast of Tohoku  
580 Earthquake. *Earth, Planets and Space*, 63, 803–808.  
581 <https://doi.org/10.5047/eps.2011.06.005>
- 582 Maeda, T., Takemura, S., & Furumura, T. (2017). OpenSWPC: An open-source integrated  
583 parallel simulation code for modeling seismic wave propagation in 3D heterogeneous  
584 viscoelastic media 4. *Seismology. Earth, Planets and Space*, 69, 102.  
585 <https://doi.org/10.1186/s40623-017-0687-2>

- 586 Matsumoto, H., Inoue, S., & Ohmachi, T. (2012). Dynamic response of bottom water pressure  
587 due to the 2011 Tohoku earthquake. *Journal of Disaster Research*, 7, 468–475.  
588 <https://doi.org/10.20965/jdr.2012.p0468>
- 589 Matsumoto, H., Nosov, M. A., Kolesov, S. V., & Kaneda, Y. (2017). Analysis of pressure and  
590 acceleration signals from the 2011 Tohoku earthquake observed by the DONET  
591 seafloor network. *Journal of Disaster Research*, 12, 163–175.  
592 <https://doi.org/10.20965/jdr.2017.p0163>
- 593 Matsumoto, K., Takanezawa, T., & Ooe, M. (2000). Ocean tide models developed by  
594 assimilating TOPEX/POSEIDON altimeter data into hydrodynamical model: A global  
595 model and a regional model around Japan. *Journal of Oceanography*, 56, 567–581.  
596 <https://doi.org/10.1023/A:1011157212596>
- 597 Melgar, D., & Hayes, G. P. (2019). Characterizing large earthquakes before rupture is complete.  
598 *Science Advances*, 5, eaav2032. <https://doi.org/10.1126/sciadv.aav2032>
- 599 Mikada, H., Mitsuzawa, K., Matsumoto, H., Watanabe, T., Morita, S., Otsuka, R., ... Suyehiro,  
600 K. (2006). New discoveries in dynamics of an M8 earthquake-phenomena and their  
601 implications from the 2003 Tokachi-oki earthquake using a long term monitoring  
602 cabled observatory. *Tectonophysics*, 426, 95–105.  
603 <https://doi.org/10.1016/j.tecto.2006.02.021>
- 604 Mikumo, T., Olsen, K. B., Fukuyama, E., & Yagi, Y. (2003). Stress-breakdown time and slip-  
605 weakening distance inferred from slip-velocity functions on earthquake faults. *Bulletin*  
606 *of the Seismological Society of America*, 93, 264–282.  
607 <https://doi.org/10.1785/0120020082>
- 608 Mizutani, A., Yomogida, K., & Tanioka, Y. (2020). Early tsunami detection with near-fault  
609 ocean-bottom pressure gauge records based on the comparison with seismic data at  
610 common sites Key Points : *Journal of Geophysical Research: Oceans*, 125,  
611 e2020JC016275. <https://doi.org/10.1029/2020JC016275>
- 612 Nakamura, T., & Hayashimoto, N. (2019). Rotation motions of cabled ocean-bottom seismic  
613 stations during the 2011 Tohoku earthquake and their effects on magnitude estimation  
614 for early warnings. *Geophysical Journal International*, 216, 1413–1427.  
615 <https://doi.org/10.1093/gji/ggy502>
- 616 Nemoto, M., Yokota, T., Takase, S., & Imamura, F. (2019). Re-examination of the tsunami  
617 source model of the 2011 off Pacific coast of Tohoku earthquake –an estimation fully  
618 using available data of tsunami-related observation–. *Journal of Japan Association of*  
619 *Earthquake Engineering*, 19, 2\_25–2\_41 (in Japanese with English abstract).  
620 [https://doi.org/10.5610/jaee.19.2\\_25](https://doi.org/10.5610/jaee.19.2_25)
- 621 Nosov, M. A., & Kolesov, S. V. (2007). Elastic oscillations of water column in the 2003  
622 Tokachi-oki tsunami source: in-situ measurements and 3-D numerical modelling.

- 623 *Natural Hazards and Earth System Science*, 7, 243–249. <https://doi.org/10.5194/nhess->  
624 7-243-2007
- 625 Okada, Y., Kasahara, K., Hori, S., Obara, K., Sekiguchi, S., Fujiwara, H., & Yamamoto, A.  
626 (2004). Recent progress of seismic observation networks in Japan - Hi-net, F-net, K-  
627 NET and KiK-net. *Earth, Planets and Space*, 56, xv–xxviii.  
628 <https://doi.org/10.1186/BF03353076>
- 629 Saito, T. (2019). *Tsunami Generation and Propagation*. Tokyo: Springer Japan.  
630 <https://doi.org/10.1007/978-4-431-56850-6>
- 631 Saito, T., & Tsushima, H. (2016). Synthesizing ocean bottom pressure records including seismic  
632 wave and tsunami contributions: Toward realistic tests of monitoring systems. *Journal*  
633 *of Geophysical Research: Solid Earth*, 121, 8175–8195.  
634 <https://doi.org/10.1002/2016JB013195>
- 635 Saito, T., & Kubota, T. (2020). Tsunami modeling for the deep sea and inside focal areas.  
636 *Annual Review of Earth and Planetary Sciences*, 48, 121–145.  
637 <https://doi.org/10.1146/annurev-earth-071719-054845>
- 638 Saito, T., Ito, Y., Inazu, D., & Hino, R. (2011). Tsunami source of the 2011 Tohoku-Oki  
639 earthquake, Japan: Inversion analysis based on dispersive tsunami simulations.  
640 *Geophysical Research Letters*, 38, L00G19. <https://doi.org/10.1029/2011GL049089>
- 641 Satake, K., Fujii, Y., Harada, T., & Namegaya, Y. (2013). Time and space distribution of  
642 coseismic slip of the 2011 Tohoku earthquake as inferred from Tsunami waveform  
643 data. *Bulletin of the Seismological Society of America*, 103(2B), 1473–1492.  
644 <https://doi.org/10.1785/0120120122>
- 645 Sato, M., Ishikawa, T., Ujihara, N., Yoshida, S., Fujita, M., Mochizuki, M., & Asada, A. (2011).  
646 Displacement above the hypocenter of the 2011 Tohoku- Oki Earthquake. *Science*,  
647 332, 1395. <https://doi.org/10.1126/science.1207401>
- 648 Suzuki, K., Hino, R., Ito, Y., Yamamoto, Y., Suzuki, S., Fujimoto, H., ... Kaneda, Y. (2012).  
649 Seismicity near the hypocenter of the 2011 off the Pacific coast of Tohoku earthquake  
650 deduced by using ocean bottom seismographic data. *Earth, Planets and Space*, 64,  
651 1125–1135. <https://doi.org/10.5047/eps.2012.04.010>
- 652 Takagi, R., Uchida, N., Nakayama, T., Azuma, R., Ishigami, A., Okada, T., ... Shiomi, K.  
653 (2019). Estimation of the orientations of the S-net cabled ocean-bottom sensors.  
654 *Seismological Research Letters*, 90, 2175–2187. <https://doi.org/10.1785/0220190093>
- 655 Tsushima, H., Hirata, K., Hayashi, Y., Tanioka, Y., Kimura, K., Sakai, S., ... Maeda, K. (2011).  
656 Near-field tsunami forecasting using offshore tsunami data from the 2011 off the  
657 Pacific coast of Tohoku Earthquake. *Earth, Planets and Space*, 63(7), 821–826.  
658 <https://doi.org/10.5047/eps.2011.06.052>

- 659 Tsushima, H., Hino, R., Tanioka, Y., Imamura, F., & Fujimoto, H. (2012). Tsunami waveform  
660 inversion incorporating permanent seafloor deformation and its application to tsunami  
661 forecasting. *Journal of Geophysical Research*, *117*, B03311.  
662 <https://doi.org/10.1029/2011JB008877>
- 663 Yamazaki, Y., Cheung, K. F., & Lay, T. (2018). A self-consistent fault slip model for the 2011  
664 Tohoku earthquake and tsunami. *Journal of Geophysical Research: Solid Earth*,  
665 *123*(2), 1435–1458. <https://doi.org/10.1002/2017JB014749>
- 666 Vigny, C., Socquet, A., Peyrat, S., Ruegg, J.-C., Métois, M., Madariaga, R., ... Kendrick, E.  
667 (2011). The 2010 Mw 8.8 Maule Megathrust Earthquake of Central Chile, Monitored  
668 by GPS. *Science*, *332*, 1417–1422. <https://doi.org/10.1126/science.1204132>
- 669 Wang, K., Sun, T., Brown, L., Hino, R., Tomita, F., Kido, M., ... Fujiwara, T. (2018). Learning  
670 from crustal deformation associated with the M9 2011 Tohoku-oki earthquake.  
671 *Geosphere*, *14*, 1–20. <https://doi.org/10.1130/GES01531.1>
- 672 Webb, S. C. (1998). Broadband seismology and noise under the ocean. *Reviews of Geophysics*,  
673 *36*, 105–142. <https://doi.org/10.1029/97RG02287>
- 674 Webb, S. C., & Nooner, S. L. (2016). High-resolution seafloor absolute pressure gauge  
675 measurements using a better counting method. *Journal of Atmospheric and Oceanic*  
676 *Technology*, *33*, 1859–1874. <https://doi.org/10.1175/JTECH-D-15-0114.1>
- 677 Wessel, P., Luis, J. F., Uieda, L., Scharroo, R., Wobbe, F., Smith, W. H. F., & Tian, D. (2019).  
678 The Generic Mapping Tools Version 6. *Geochemistry, Geophysics, Geosystems*, *20*,  
679 5556–5564. <https://doi.org/10.1029/2019GC008515>
- 680

Figure 1.

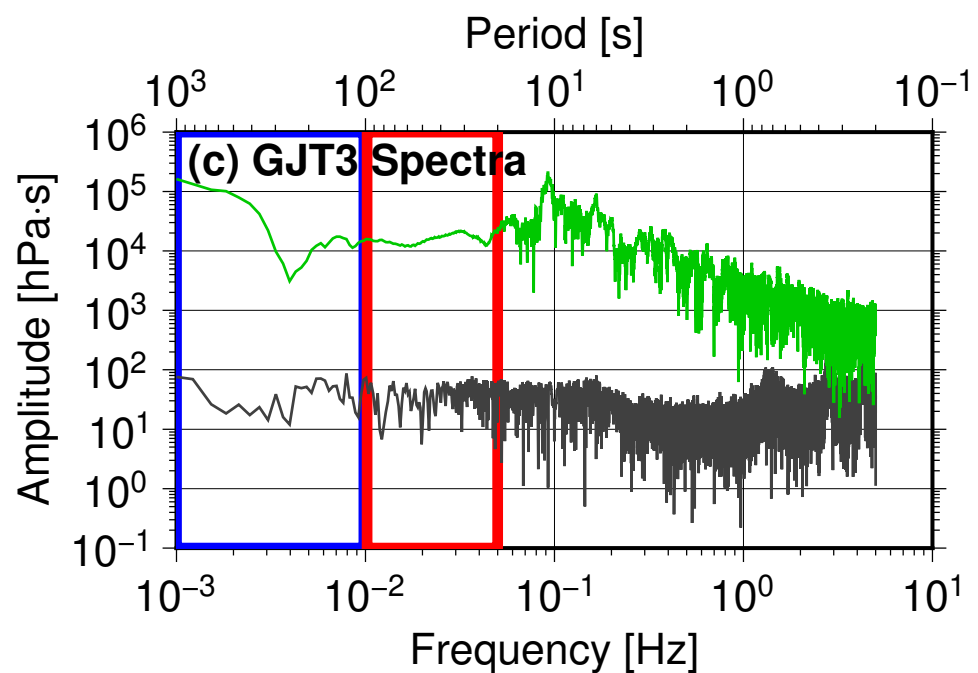
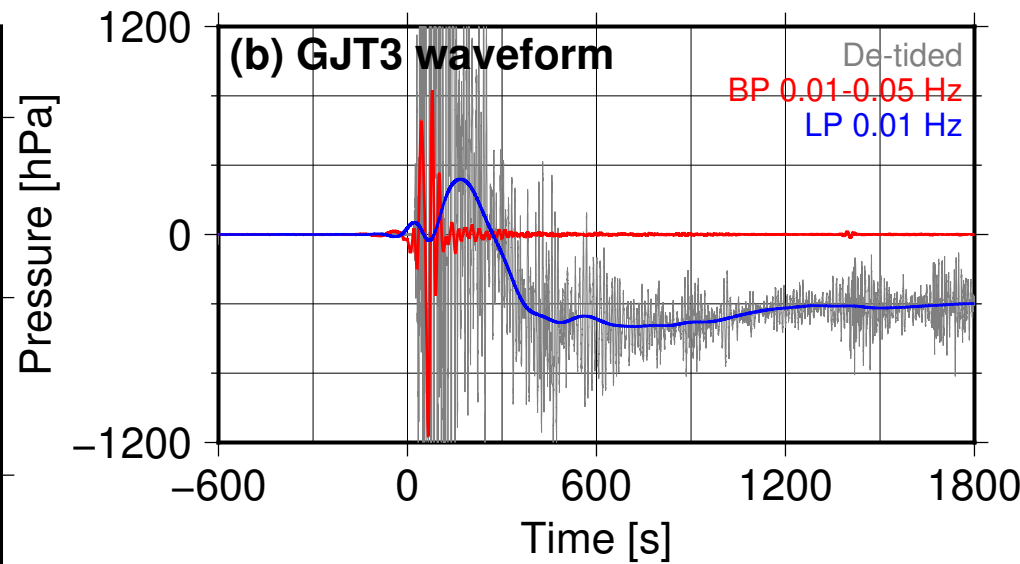
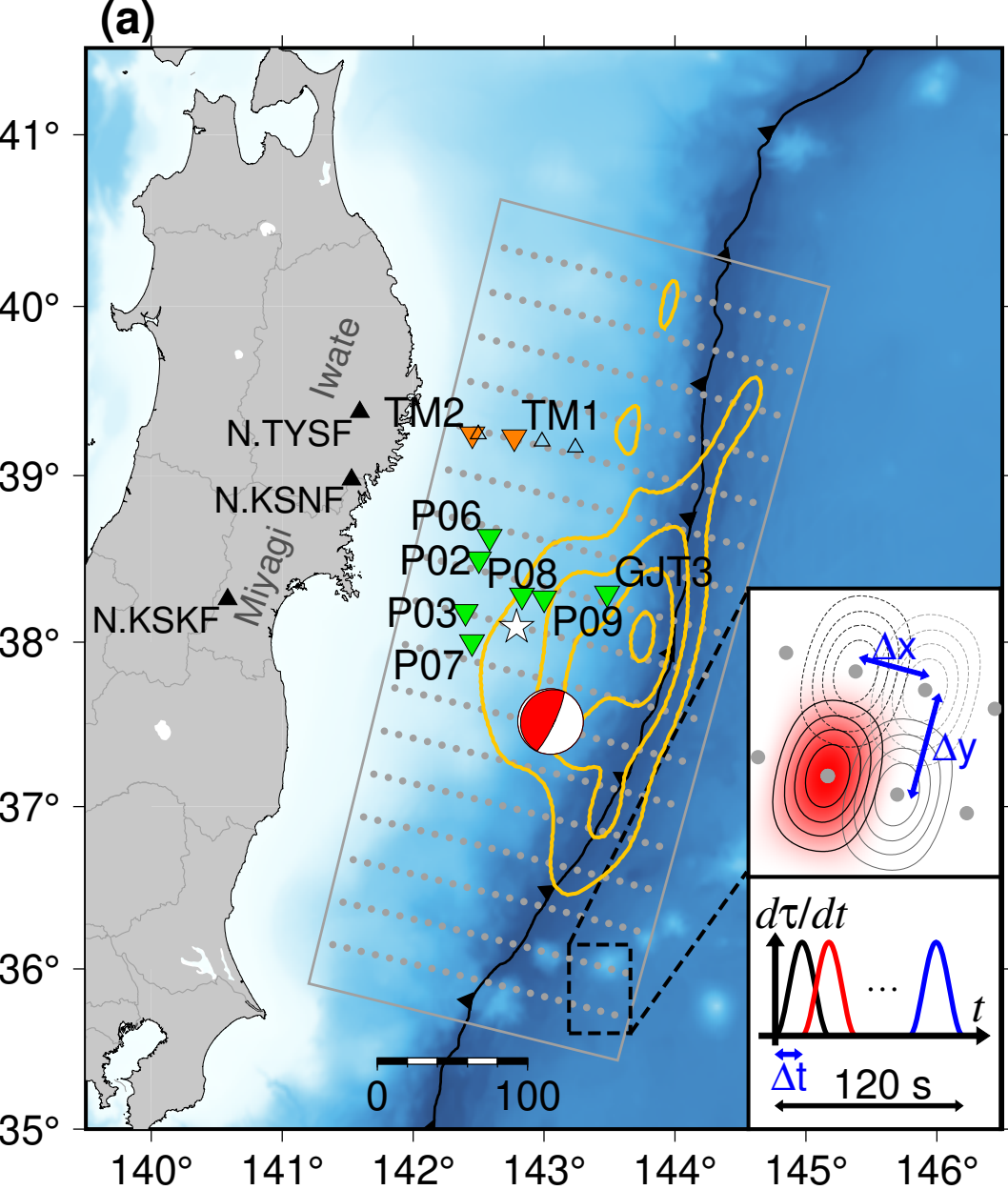


Figure 2.

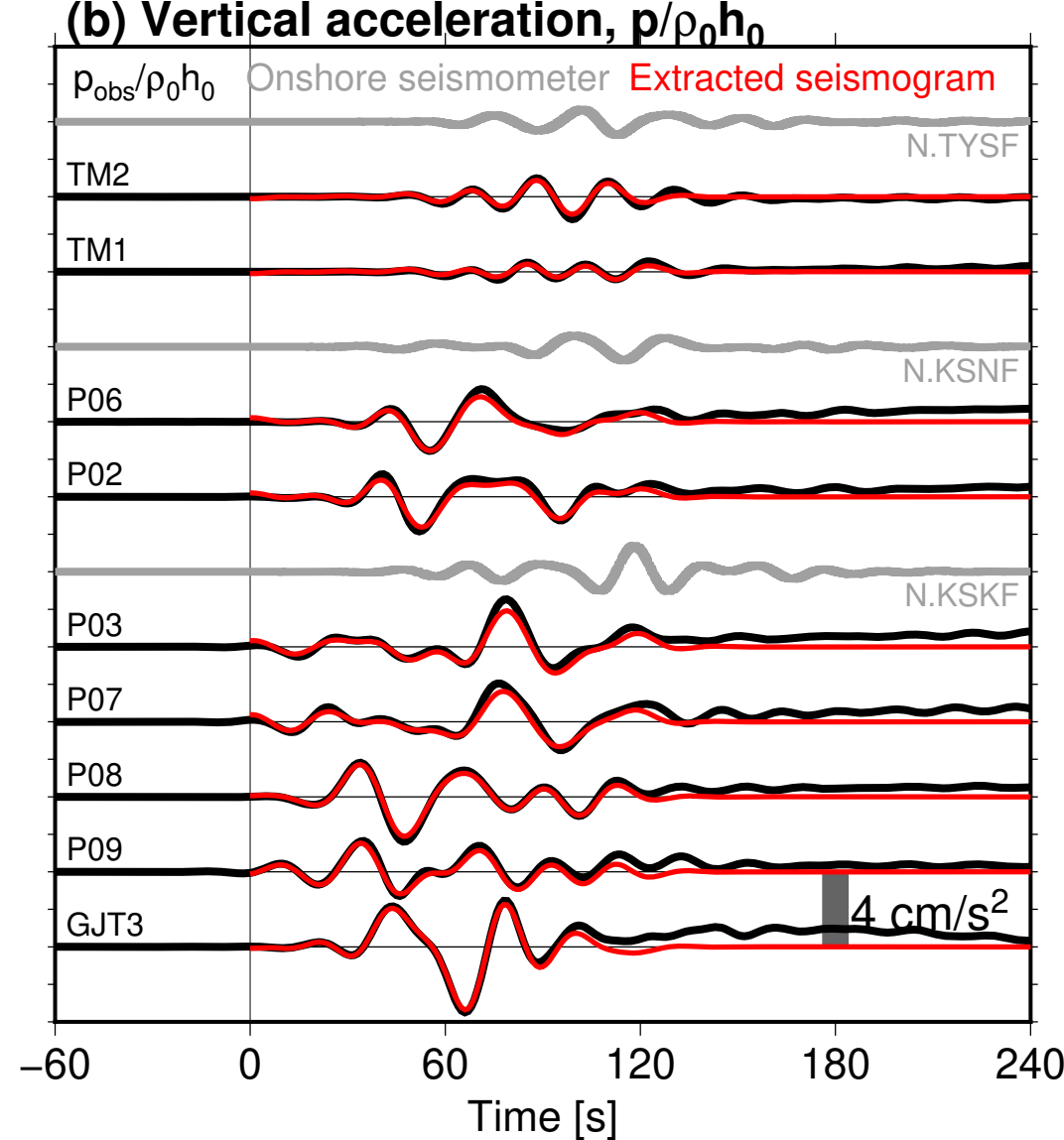
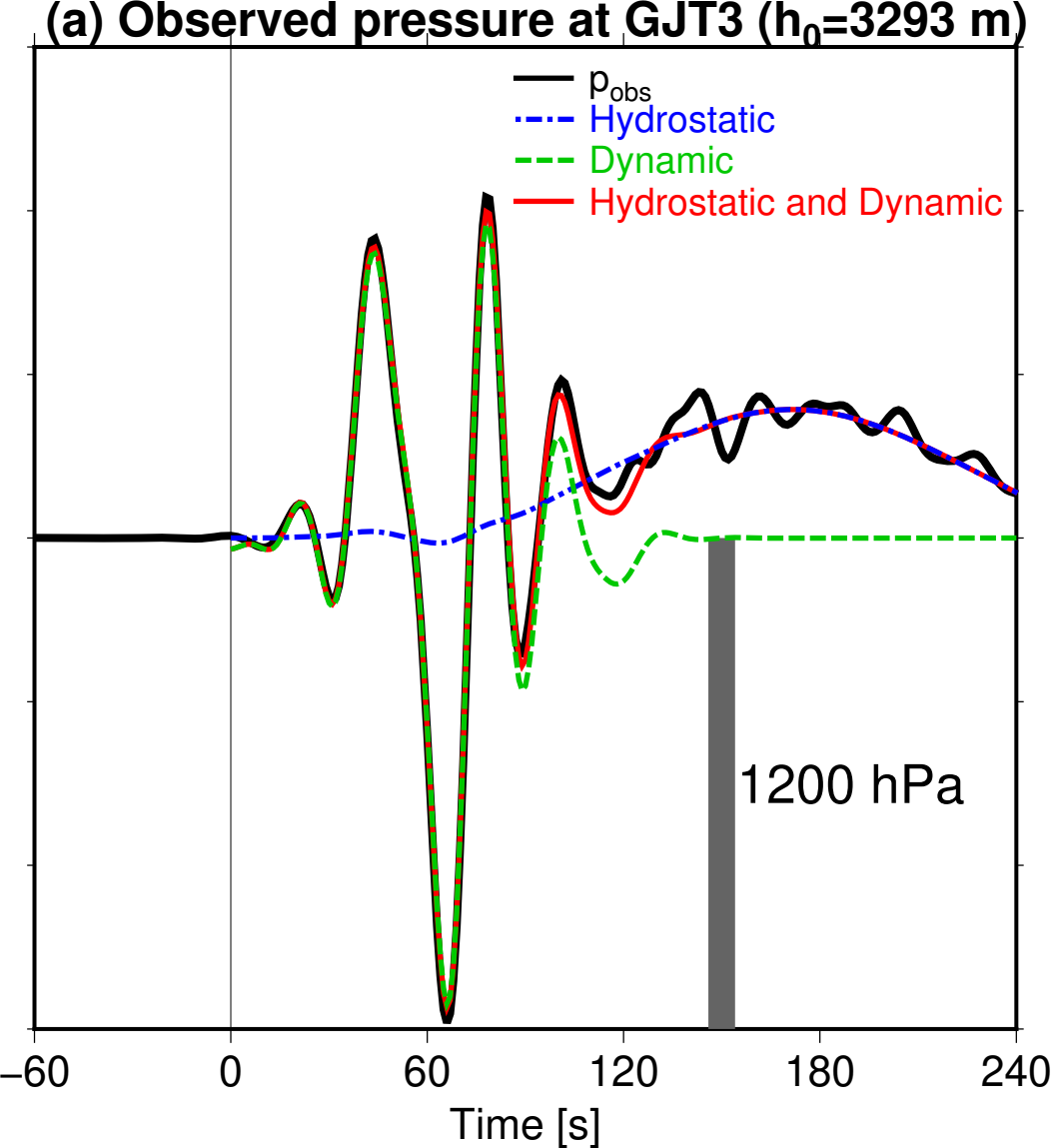


Figure 3.

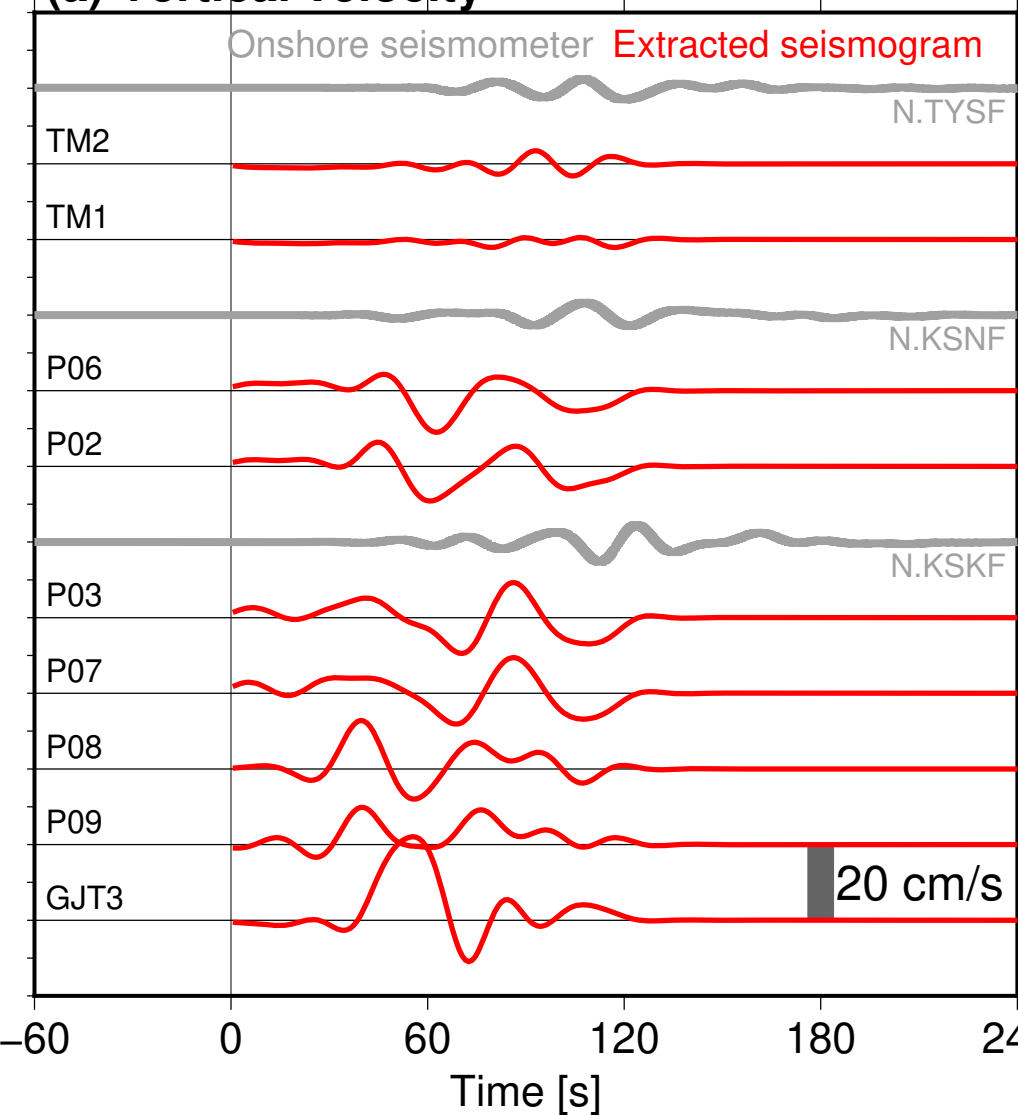
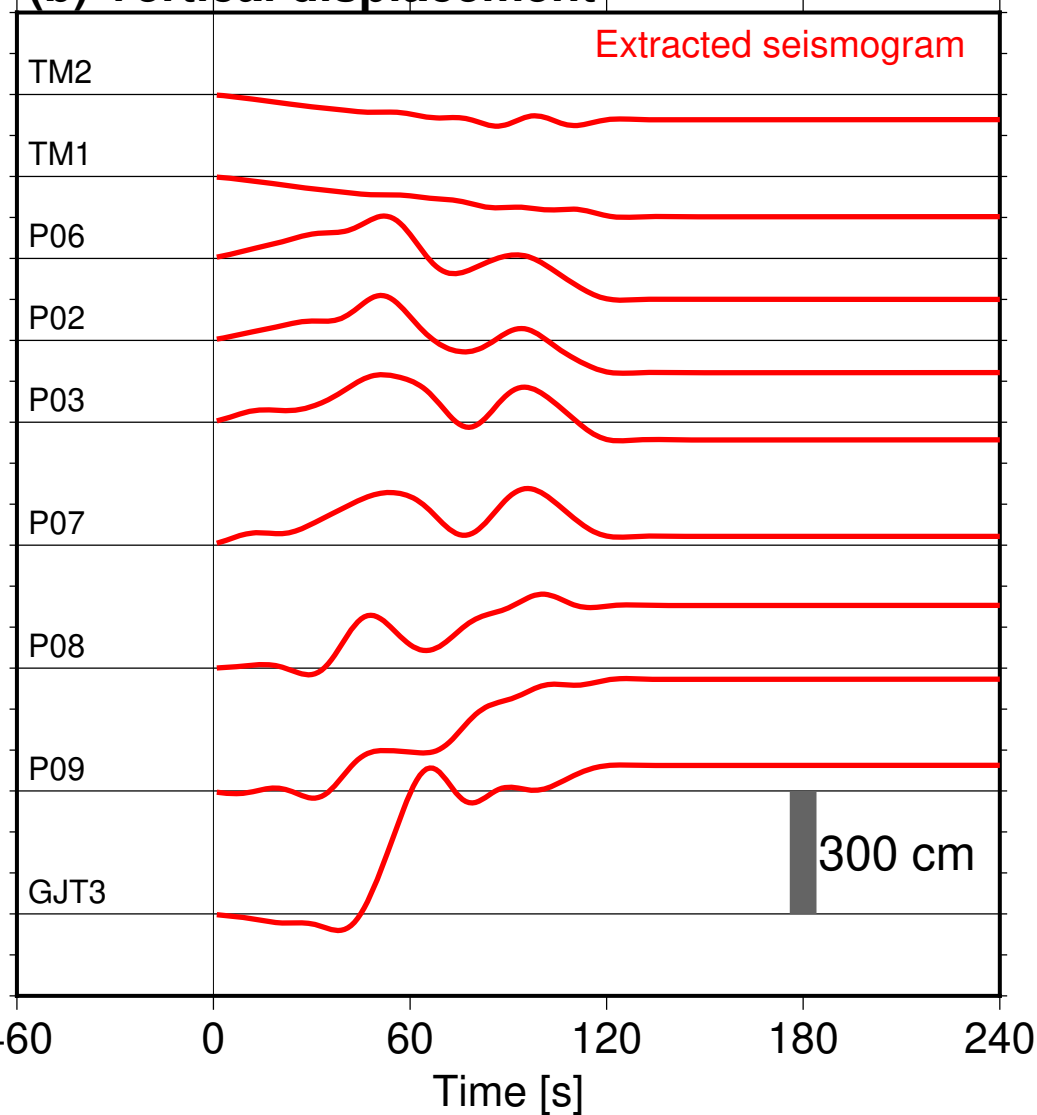
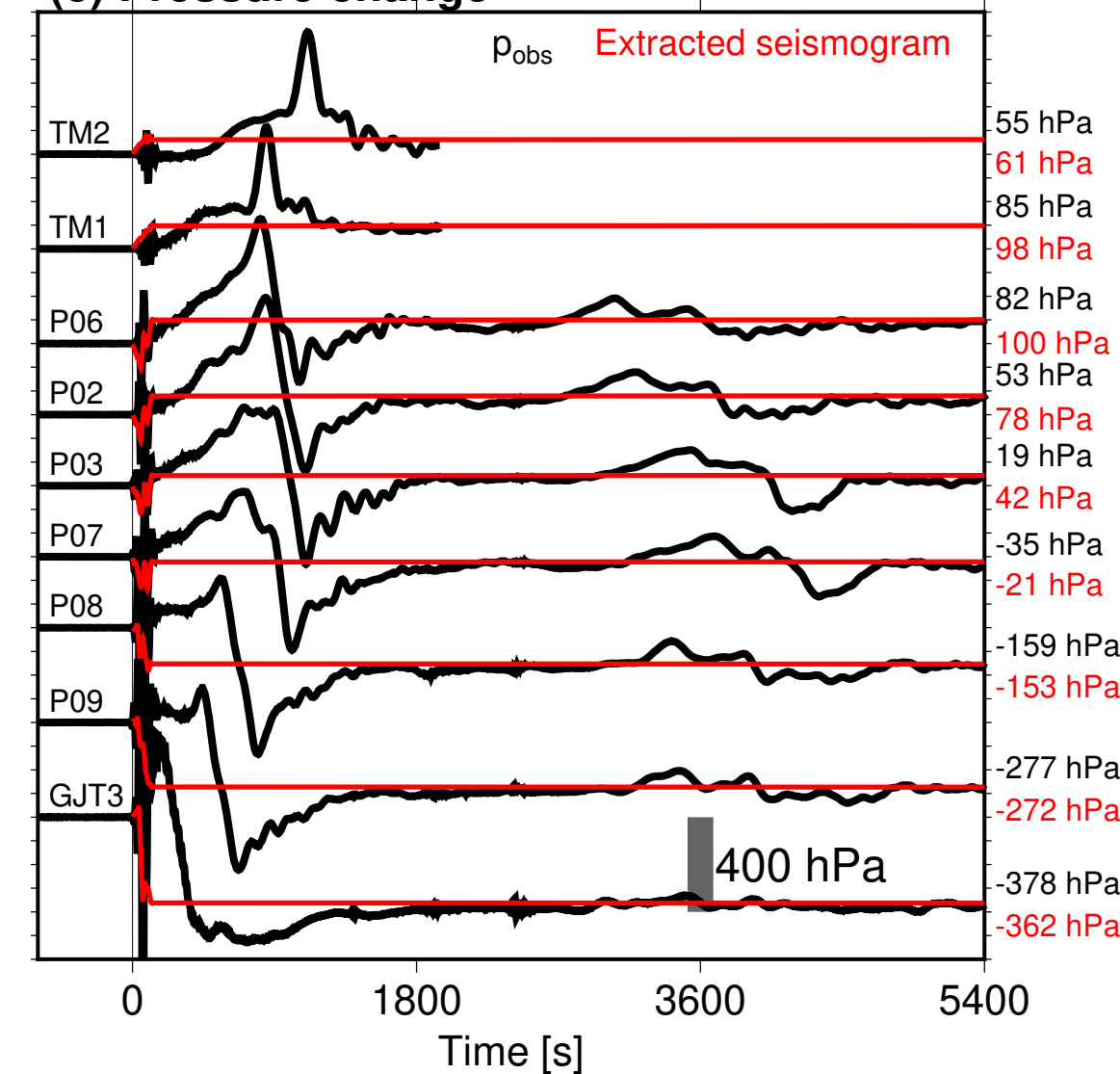
**(a) Vertical velocity****(b) Vertical displacement****(c) Pressure change**

Figure 4.

